nature communications

Article

https://doi.org/10.1038/s41467-025-59561-0

Surprising pressure-induced magnetic transformations from helimagnetic order to antiferromagnetic state in NiI_2

Received: 6 May 2024

Accepted: 28 April 2025

Published online: 07 May 2025

Check for updates

Qiye Liu[1,2,9], Wenjie Su[2,9], Yue Gu[3,9], Xi Zhang[2], Xiuquan Xia[2], Le Wang[2], Ke Xiao[4], Naipeng Zhang[2], Xiaodong Cui[5], Mingyuan Huang[2], Chengrong Wei[6], Xiaolong Zou[7] ✉, Bin Xi[8] ✉, Jia-Wei Mei[2] ✉ & Jun-Feng Dai[1,2] ✉

Interlayer magnetic interactions play a pivotal role in determining the magnetic arrangement within van der Waals (vdW) magnets, and the remarkable tunability of these interactions through applied pressure further enhances their significance. Here, we investigate NiI_2 flakes, a representative vdW magnet, under hydrostatic pressures up to 11 GPa. We reveal a notable increase in magnetic transition temperatures for both helimagnetic and antiferromagnetic states, and find that a reversible transition between helimagnetic and antiferromagnetic (AFM) phases at approximately 7 GPa challenges established theoretical and experimental expectations. While the increase in transition temperature aligns with pressure-enhanced overall exchange interaction strengths, we identify the significant role of the second-nearest neighbor interlayer interaction $J_2^{\perp}$, which competes with intra-layer frustration and favors the AFM state as demonstrated in the Monte Carlo simulations. Experimental and simulated results converge on the existence of an intermediate helimagnetic ordered state in NiI_2 before transitioning to the AFM state. These findings underscore the pivotal role of interlayer interactions in shaping the magnetic ground state, providing fresh perspectives for innovative applications in nanoscale magnetic device design.

In the domains of condensed matter physics and materials science, van der Waals (vdW) magnets have emerged as an intellectually captivating frontier, revealing a rich tapestry of magnetic phenomena that has ignited profound interest and exploration[1–5]. The complexity and richness of magnetic behaviors within vdW magnets become increasingly prominent as one delves into the intricate interplay among adjacent layers, characterized by a diverse array of interlayer couplings[6–9]. These interlayer couplings, spanning from van der Waals to magnetic interactions, not only govern the magnetic ground state but also bestow upon these materials an extraordinary degree of

[1]College of Integrated Circuits and Optoelectronic Chips, Shenzhen Technology University, Shenzhen 518118, China. [2]Department of Physics and Shenzhen Institute for Quantum Science and Engineering, Southern University of Science and Technology, Shenzhen 518055, China. [3]State Key Laboratory of Low Dimensional Quantum Physics and Department of Physics, Tsinghua University, Beijing, China. [4]NISE Department, Max Planck Institute of Microstructure Physics, Halle, Germany. [5]Physics Department, The University of Hong Kong, Pokfulam Road, Hong Kong, China. [6]College Physics Teaching and Experiment Center, Shenzhen Technology University, Shenzhen 518118, China. [7]Shenzhen Geim Graphene Center, Tsinghua-Berkeley Shenzhen Institute & Tsinghua Shenzhen International Graduate School, Tsinghua University, Shenzhen 518055, China. [8]College of Physics Science and Technology, Yangzhou University, Yangzhou 225002, China. [9]These authors contributed equally: Qiye Liu, Wenjie Su, Yue Gu. ✉e-mail: xlzou@sz.tsinghua.edu.cn; xibin@yzu.edu.cn; meijw@sustech.edu.cn; daijunfeng@sztu.edu.cn

tunability. This inherent versatility renders vdW magnets multifaceted and holds the tantalizing potential for groundbreaking applications. The precision control of interlayer coupling is attainable through diverse strategies, encompassing the manipulation of stacking order[10,11], gate tuning[12–14], and the application of pressure[15,16].

Transition metal dihalides, exemplified by NiI_2, have emerged as subjects of keen interest, owing to their intricate magnetic behaviors and the potential manifestation of multiferroic properties[17]. In the single-layer configuration, each Ni^{2+} bonds with six I^- to form an octahedral NiI_6^{4-} structure. Three such single-layers are stacked along the c-axis, resulting in a $CdCl_2$-type layered structure with a centrosymmetric space group[18]. Specific heat capacity and magnetic susceptibility measurements (Fig. 1a) on NiI_2 single crystals reveal two distinct phase transitions during the cooling process, occurring at approximately 73 K (T_{N1}) and 60 K (T_{N2})[19]. At T_{N1}, NiI_2 undergoes a magnetic phase transition from a paramagnetic to colinear antiferromagnetic state, still maintaining centrosymmetric $R\bar{3}m$ space group[20]. Below T_{N2}, a spiral antiferromagnetic order emerges, characterized by a transition in structure from trigonal to monoclinic. the spins rotate within the plane perpendicular to the propagation vector $\mathbf{q}\sim$ (0.138, 0, 1.457), slanted at an angle of ~55 degrees from the *c*-axis (left figure in Fig. 1b)[21]. Consequently, the helimagnetic state induces spontaneous electric polarization due to the inverse Dzyaloshinskii–Moriya (DM) interaction, as validated by polarization current measurements under an in-plane magnetic field[22]. Consequently, NiI_2 has been postulated to possess a multiferroic ground state, primarily attributed to its robust magnetoelectric (ME) effect. Recent debates have revolved around whether this multiferroic state can persist in NiI_2 down to the monolayer limit[23–26].

The presence of a helical spin configuration in non-chiral centrosymmetric crystals alludes to the complex exchange interactions among adjacent magnetic atoms in NiI_2, stemming primarily from inherent geometric frustration and the presence of a frustrated Kitaev interaction[27]. The ease of tunability between various magnetic states in NiI_2 is expected to be governed by the inter-layer couplings (Fig. 1b). To this end, we subjected NiI_2 flakes, serving as representative vdW magnets, to hydrostatic pressures of up to 11 GPa. This approach enabled us to embark on a comprehensive investigation into the intricate role of van der Waals interlayer magnetic interactions, furthering our understanding of the competition among different alignments of magnetic spins. Under these meticulously controlled pressure conditions, we observed a noteworthy increase in the magnetic transition temperatures for both helimagnetic and antiferromagnetic states under low pressures. Notably, a striking and reversible transition between a helimagnetic and an antiferromagnetic state was noted at approximately 7 GPa. Our Monte Carlo simulations and reported Density Functional Theory calculations offered valuable insights, revealing the rapid strengthening of interlayer interactions under pressure. This phenomenon led to the enhancement of transition temperatures and, consequently, the observed transition from a helimagnetic to an antiferromagnetic state. These findings underscore the pivotal role played by interlayer interactions in shaping the magnetic ground state.

Results and discussion

Enhanced magnetic transition temperatures under low pressures

The hydrostatic pressure was applied to the samples using a diamond-anvil cell (DAC) technique, which allowed us to achieve pressures of up to 20 GPa. Initially, NiI_2 flakes (50–100 nm) were mechanically exfoliated and then delicately transferred onto the culet of the diamond using a dry transfer method[28]. Subsequently, we introduced a pressure-transmitting medium, namely silicone oil, into the gasket blanks. The DAC was assembled by aligning and securing the two diamonds with four screws. Notably, this entire procedure was conducted within a nitrogen-filled glove box to prevent any degradation of the samples.

Temperature-dependent Raman measurements and polarization-sensitive second harmonic generation (SHG) were carried out in a back-reflected geometry under applied pressures, capitalizing on the excellent transparency and low polarization response of diamond. These techniques were significant in determining the magnetic transition temperatures. The Raman measurements allowed us to extract the intensity evolution of the phonon mode related to collinear antiferromagnetic orders as temperatures varied and ascertain the transition temperature. Additionally, polarization-resolved and temperature-dependent SHG spectra were obtained to probe the inversion-symmetry-breaking features of the spin structure under pressure, yielding insights into the transition temperature to the helimagnetic state. (For detailed information regarding the experimental setup, please refer to the "Methods" section and Fig. S1.)

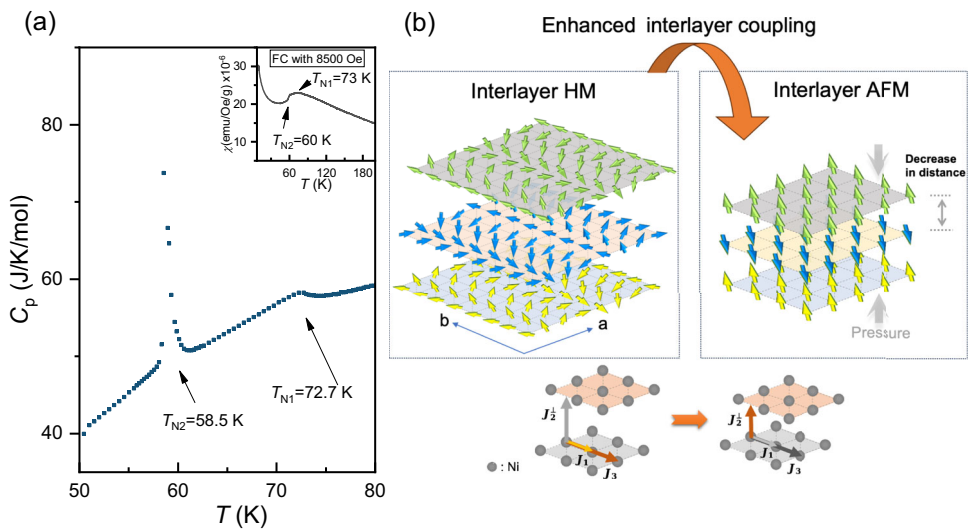

Fig. 1 | Magnetic ordering and properties of layered NiI_2. a Specific heat capacity and magnetic susceptibility of NiI_2 as a function of temperature. FC stands for field cooling. **b** Schematic illustration of the transition of magnetic structure in NiI_2, shifting from helimagnetic (HM) to antiferromagnetic (AFM) states due to enhanced interlayer coupling. Lower figure represents the dominate interlayer exchange interactions J_1 and J_3 at ambient pressure and the perpendicular effective exchange coupling $J_2^{\perp}$ at high pressure.

https://doi.org/10.1038/s41467-025-59561-0

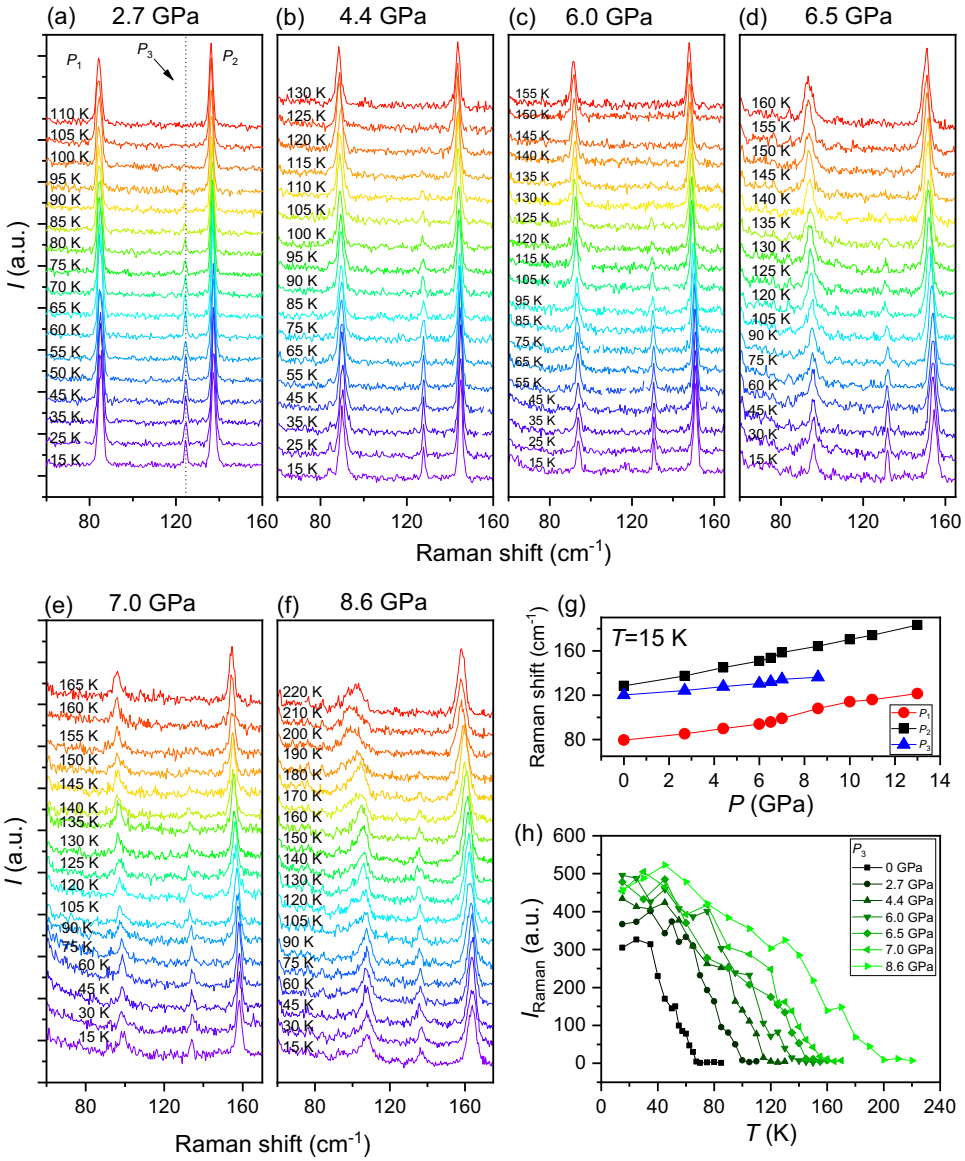

Fig. 2 | Raman spectra of NiI_2 under different pressures. a–f Raman spectra of NiI_2 flake at different temperatures under various pressures, e.g., 2.7, 4.4, 6.0, 6.5, 7.0, and 8.6 GPa. The dotted line in (**a**) indicates the peak of the zone-folded phonon mode (P_3). **g** Raman shifts of P_1, P_2, and P_3 peaks as a function of pressure. **h** The integrated intensity of P_3 peak as a function of temperature under 0, 2.7, 4.4, 6.0, 6.5, 7.0, and 8.6 GPa, respectively.

We conducted temperature-dependent Raman measurements on a NiI_2 flake, utilizing an excitation centered at 1.96 eV. Under ambient pressure, six distinct Raman peaks were observed at 15 K (Fig. S2), in line with previously reported findings in the literature[25]. Of particular interest is the Raman mode (P_3) at 120 cm^{-1}, where its intensity displays a significant temperature dependence. Specifically, the intensity gradually reduces as the temperature increases, ultimately vanishing between the Néel temperature transition points (T_{N1} and T_{N2}). To verify the origin of the 120 cm^{-1} Raman mode, we conducted Raman measurements on NiI_2 flakes under an out-of-plane magnetic field of up to 8 T (the results are shown in Fig. S3). Surprisingly, we did not observe any shift or splitting in this mode, suggesting it is not a magnon mode. The possible origin of this peak appears to be zone folding due to the presence of antiferromagnetic order. As described in ref. 20, NiI_2 exhibits a canted interlayer antiferromagnetic structure with ferromagnetic alignment within layers below T_{N1}. This magnetic arrangement induces Brillouin zone folding along the z-direction by the magnetic cell doubling, thereby making the specific Raman modes active. However, further experiments, such as high-resolution Raman scattering under controlled magnetic fields, are required to fully elucidate the origin of the 120 cm^{-1} mode. Nevertheless, Raman measurements provide a reliable means to estimate the Néel temperature, despite a slightly lower temperature reading compared to values obtained through thermodynamic measurements.

Figure 2a–f provides a visual representation of our temperature-dependent Raman results under various hydrostatic pressures. At 15 K, two phonon modes (P_1 and P_2) and a zone-folded phonon mode (P_3) exhibit a linear blueshift as pressure increases (Figs. 2g and S4), an effect attributed to enhanced interlayer coupling. Importantly, the absence of new Raman peaks indicates the structural stability of the crystal below 13 GPa. However, it is worth noting that as reported in references[29–31], the structure of NiI_2 begins to collapse when the pressure exceeds 19 GPa. The temperature-dependent integrated intensity of the P_3 peak under varying pressure conditions is plotted in Fig. 2h. Notably, our observations reveal the remarkable resilience of the zone-folded phonon signals even under elevated pressures and increased

https://doi.org/10.1038/s41467-025-59561-0

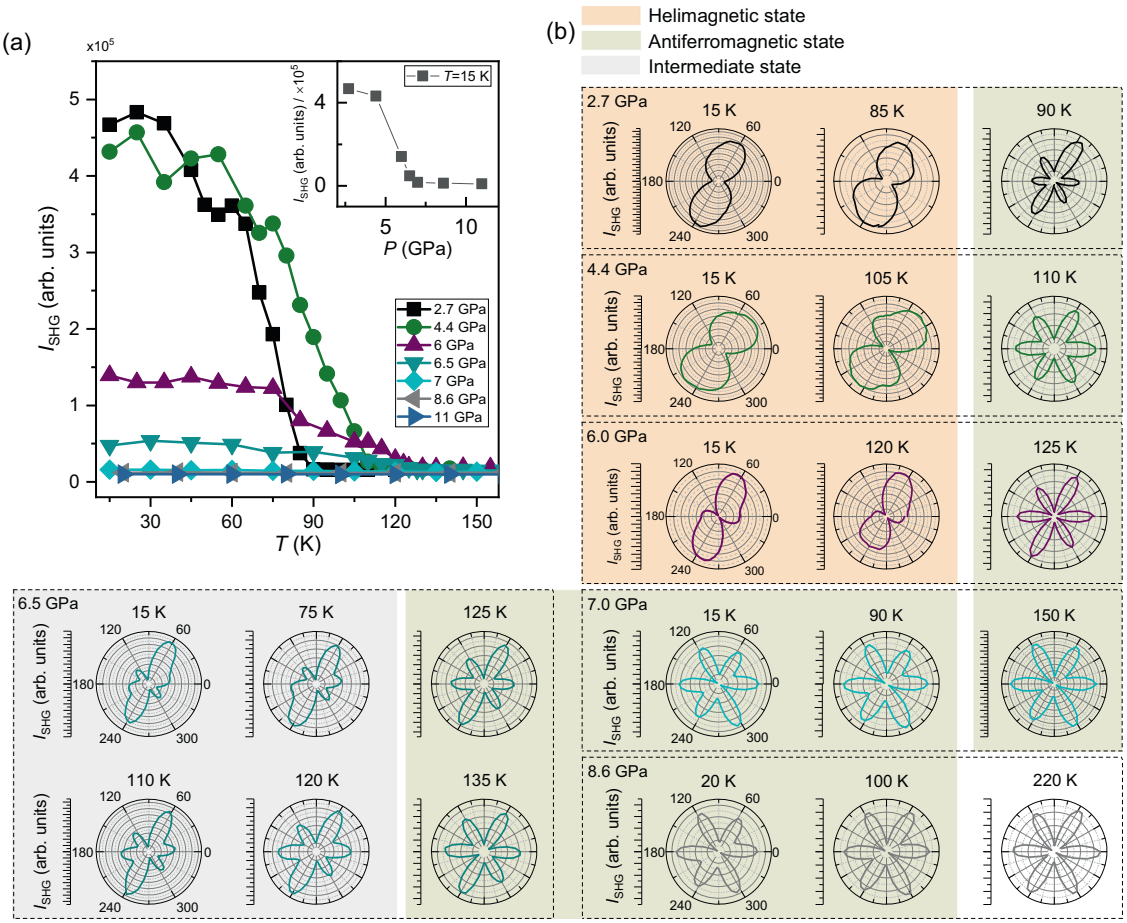

Fig. 3 | SHG in NiI_2 under different pressures. a Temperature-dependent SHG intensity in a NiI_2 flake at seven fixed hydrostatic pressures, e.g., 2.7, 4.4, 6.0, 6.5, 7.0, 8.6, and 11.0 GPa. The inset shows the pressure dependence of the SHG intensity at approximately 15 K. **b** Angular-resolved SHG patterns for temperatures below and above the helimagnetic transition temperature at the six representative hydrostatic pressures. Here, the orange, green, and gray regions represent the helimagnetic state (HM), antiferromagnetic state (AFM) and intermediate state (IMS), respectively.

temperatures. For instance, at 2.7 GPa, the P_3 peak persists at 100 K, and it continues to endure at 115 K under 4.4 GPa, and at 135 K under 6.0 GPa. Surprisingly, at even higher pressures, such as 7 and 8.6 GPa, the P_3 peak remain discernible, with their transition temperature showing a remarkable increase, reaching 155 K at 7 GPa and 200 K at 8.6 GPa. It underlines the robustness of the antiferromagnetic state, illustrating its resilience against the influence of pressure. In the ref. 29, the pressure-induced enhancement of the magnetic transition temperature has also demonstrated using Mössbauer spectroscopy, where the Néel temperature increased to 310 K at 19 GPa. This phenomenon has also been reported in other vdW magnets, such as $CrSi(Ge)Te_3$[32,33].

At room temperature and atmospheric pressure, NiI_2, characterized by a centrosymmetric space group, inherently exhibits an electric-dipole forbidden second harmonic generation (SHG). However, below the Néel temperature T_{N2}, a phase transition occurs, leading to the emergence of helimagnetic orders. This transition signifies the breaking of both spatial inversion and time-reversal symmetries, thereby enabling SHG induced by magnetism. We observe a distinct and robust SHG signal at temperatures below 59 K (Fig. S5a), reaching magnitudes up to two orders of magnitude greater than those observed at elevated temperatures. This pronounced SHG signal indicates the presence of a helical spin structure beneath the transition temperature, a characteristic that is consistent with the transition temperature T_{N2} determined by the magnetic susceptibility measurement. Moreover, the polarization-dependent SHG measurement shows that the SHG intensity at 15 K reveals a strong signal in the *XY* configuration, manifesting as a distorted "8" pattern, while the *XX* configuration exhibits a relatively weaker signal characterized by a distorted butterfly pattern. Here, the *XX* and *XY* configurations indicate that the orientation of the SHG signal is parallel and perpendicular to the polarization of the incident light, respectively. Both SHG patterns unveil a two-fold symmetry in NiI_2 induced by the contribution of both electric and magnetic dipoles below T_{N2} (Fig. S5b), indicating a mirror symmetry breaking. Furthermore, the polarization-dependent SHG at 65 K reveals a distinctive six-fold rotational symmetry under high-power excitation (Fig. S5b). This symmetry reflects a C_3 symmetry, signifying that NiI_2 has transitioned to a collinear antiferromagnetic order characterized by spatial inversion symmetry. It may originate from the quadrupole term and surface electric dipole term. Consequently, SHG measurements serve as a valuable tool for delineating the phase transition from helimagnetic to collinear antiferromagnetic states.

Figure 3a presents the SHG signal intensity as a function of temperature under seven constant hydrostatic pressures. At 2.7 GPa, the SHG signal intensity undergoes a gradual change as the temperature increases from 15 to 65 K. However, it experiences a rapid and significant decrease, approaching a minimum at approximately 90 K. This shift corresponds to a remarkable alteration, with a maximum-to-minimum intensity ratio of approximately 30:1 during the temperature rise. Consequently, we can roughly identify this point as the transition temperature marking the phase transition from the helimagnetic to antiferromagnetic states under pressure. Specifically, at

https://doi.org/10.1038/s41467-025-59561-0

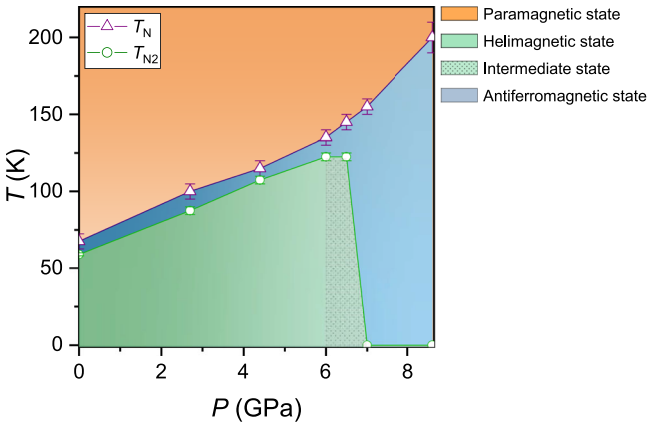

Fig. 4 | Magnetic phase diagram of NiI_2. The magnetic phase diagram of the NiI_2 flake as a function of pressure and temperature. T_N and T_{N2} are obtained from Raman and SHG measurements, respectively. Here, the orange, green region, blue, and gray regions represent the paramagnetic (PM), helimagnetic (HM), antiferromagnetic (AFM) and intermediate (IMS) states, respectively.

2.7 GPa, this transition temperature is found to be around 90 K, surpassing the 59 K recorded under atmospheric pressure. Elevating the pressure to 4.4 and 6.0 reveals a similar temperature-dependent SHG signal curve, accompanied by a corresponding increase in the transition temperature (as shown in Fig. 3a). The maximum transition temperature is determined to be 125 K at 6 GPa.

Beyond the SHG signal intensity, the SHG pattern also serves as a distinctive indicator for distinguishing between helimagnetic and antiferromagnetic states. To clarify the symmetric information, we only focus on the *XY* component in the polarization-dependent SHG measurement. As displayed in Fig. 3b, the *XY* component of the polarization-resolved SHG spectrum retains a distorted "8" pattern at both 15 K and 85 K under 2.7 GPa pressure. This signifies a two-fold symmetry that persists at lower pressures. However, at 90 K, the SHG pattern undergoes a transformation, displaying a distorted six-petal pattern indicative of C_3 symmetry. It's worth noting that the distortion may be influenced by the weak polarization response of the diamond under pressure. Thus, the transition temperature (T_{N2}) is determined to be 87.5 ± 2.5 K for NiI_2 under 2.7 GPa pressure, consistent with the value derived from the intensity-temperature relationship. At both 4.4 and 6 GPa in Fig. 2b, a noticeable difference in the SHG pattern remains evident as the temperature increases. Consequently, the transition temperature is approximated to be 107.5 ± 2.5 K at 4.4 GPa and 122.5 ± 2.5 K at 6 GPa, allowing for the identification of the maximum transition temperature from the helimagnetic to antiferromagnetic states via the SHG patterns.

Pressure-induced magnetic phase transition from HM to AFM

Remarkably, as we escalate the pressure to 7 GPa, the intensity of SHG decreases by an order of magnitude from 4.67×10^5 at 2.7 GPa to 0.16×10^5 at 7 GPa at around 15 K (the inset of Fig. 3a), while the excitation intensity remains unchanged. Beyond this point, the SHG intensity remains at its lowest value up to 11 GPa. Meanwhile, the SHG intensity at high pressures (>7 GPa) is comparable to that observed at high temperatures under low pressures (<6 GPa). This suggests the disappearance of helimagnetic order, with 7 GPa being the critical point. Moreover, the SHG intensity exhibits negligible temperature dependence within the wide range of 15–150 K (as indicated by the light green diamonds in Fig. 3a). This intriguing temperature independence is sustained even when the pressure is further raised to 8.6 and 11 GPa. To further confirm the disappearance of helimagnetic order, we also examined the SHG pattern at 7 GPa. As depicted in Fig. 3b, a distinct distorted six-petal pattern is evident for selected temperature points, including 15, 90, and 150 K. This pattern markedly differs from the previously observed distorted "8" pattern characterizing the helimagnetic state. It is noted that the distortion of SHG pattern is attributed to the interlayer sliding under high pressures, which is characteristic of typical layered materials[34]. Moreover, at this pressure, the zone-folded phonon (P_3) as shown in Fig. 2e remains observable. Hence, this transition indicates the vanishing or complete suppression of the helimagnetic state at approximately 7 GPa, with a subsequent transformation into a collinear antiferromagnetic. The same experimental phenomenon can be observed at 8.6 GPa (Fig. 3b). This further confirms a phase transition from the helimagnetic to the collinear antiferromagnetic states at high pressures. At 6.5 GPa, a notable shift is observed in the maximum-to-minimum intensity ratio of the SHG signal, reducing significantly to 4:1. It is notably lower than the value observed at 2.7 GPa. Furthermore, the SHG pattern at 15 K deviates from its previously distorted '8' pattern, exhibiting a combination of '8' and six-petal patterns. One possible explanation could be the coexistence of AFM and helimagnetic phases due to uneven pressure distribution around the phase transition point. Alternatively, the deviation may originate from an intermediate state between the helimagnetic and AFM states. We fitted the SHG pattern at 6.5 GPa and compared it with that at atmospheric pressure, as shown in Fig. S6. From these results, it is evident that the magnetic dipole term is significantly affected by the applied pressure, while the electric dipole term remains largely unchanged. This suggests that the applied pressure may significantly influence the exchange interaction, which is crucial for determining the intermediate state. The detailed magnetic structure could be clarified through the neutron scattering measurements under pressure. These alterations strongly indicate the transition from a helimagnetic to an antiferromagnetic state has occurred at this critical pressure.

As the pressure surpasses 10 GPa, the P_3 peak becomes undetectable (Fig. S4), possibly due to a reduction in the charge transfer gap that shifts the optical transitions away from the excitation wavelength[35–37]. It is noteworthy that antiferromagnetic order can persist up to 19 GPa, with an enhanced Néel temperature of 310 K, as revealed by Mössbauer spectroscopy in ref. 29. At 11 GPa, our SHG patterns, as depicted in Fig. S7, exhibit a consistent distorted six-petal pattern across the temperature range of 20–200 K, indicating the likely presence of a collinear antiferromagnetic state. In Fig. 4, we compile a comprehensive phase diagram outlining the transition from the helimagnetic state (T_{N2}) to the antiferromagnetic state (T_N) under varying pressures. Below 6 GPa, the transition temperature for the helimagnetic state (open green circles) exhibits a gradual ascent to 122.5 K with increasing pressure before transforming into an antiferromagnetic state at around 7 GPa. This transition is accompanied by an intermediate state (IMS in Fig. 4) between two pressures. Furthermore, the antiferromagnetic state endures at around 190 K under 8.6 GPa pressure from our Raman findings (purple triangles in Fig. 4). From ref. 29, the actual transition from antiferromagnetic to paramagnetic state can increase to 216 K at around 8.3 GPa. Importantly, upon releasing the pressure to 2 GPa, the reappearance of the distorted "8" pattern below 81 K (as shown in Fig. S8) underscores the pressure-controlled transition between the helimagnetic and antiferromagnetic states. This novel capability to modulate the helimagnetic state transition via pressure holds the promise of advancing innovative functional devices driven by external forces.

Monte Carlo (MC) simulations were conducted to investigate the response of the magnetic properties of NiI_2 to external pressure. Our simulation incorporates consideration of the intralayer nearest-neighbor interaction (J_1), the intralayer next-next-nearest neighbor interaction (J_3), and interlayer next-nearest neighbor interaction ($J_2^{\perp}$) as defined in ref. 38. Other small exchange interactions estimated in DFT are also added and fixed during our simulation. Detailed

https://doi.org/10.1038/s41467-025-59561-0

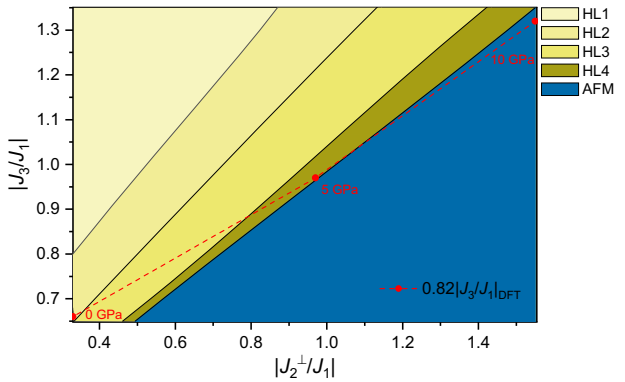

Fig. 5 | Magnetic states of NiI_2. Phase diagram encompassing all the magnetic states (HL1, HL2, HL3, HL4, and AFM, as described in Fig. S9) with differing intralayer and interlayer exchange interactions. HL2 is identified as the helimagnetic ground state for NiI_2 at low temperature. The red data points represent the exchange interaction under pressure, sourced from DFT calculations in ref. 38.

information regarding the simulation methodology can be found in the "Method" section. At ambient pressure, the helimagnetic ground state, as indicated by the HL2 (Fig. S9), is attained due to the competition between the intralayer FM interaction J_1 and the AFM interaction J_3[38]. In this state, spins rotate within the canted Ni_2I_2 plane with a propagation vector $\mathbf{Q} \approx (1/7, 0, 3/2)$, as depicted in Figs. 1b and S9. The spin configuration of the helimagnetic states is sensitive to the competition between J_1, J_3, and the intralayer interactions $J_2^{\perp}$. Varying the interlayer and intralayer interactions has yielded other helimagnetic states, denoted as HL1, HL3, and HL4 (Fig. S9), with corresponding propagation vectors (1/14, 1/14, 1/2), (1/14, 6/7, 0.5), and (0, 13/14, 0.5), respectively. Remarkably, the AFM (Figs. S9–S11) state can emerge as the dominant magnetic ground state when the interlayer interaction is strengthened, as indicated in the deep blue region of Fig. 5. It differs from the MC simulation in ref. 38 in which only the helimagnetic states are revealed under high pressure. To incorporate the DFT results of the magnetic interactions[38] into our phase diagram, we scale the DFT values of J_3 by a factor $0.82J_3$ to align with our high-pressure experimental results of the magnetic transition from the helimagnetic states to the AFM state. The DFT simulation may overestimate J_3, regarding to the fact that the MC phase boundary is sensitive to the magnetic interaction parameters. In Fig. 5, the DFT results with the scale ($0.82J_3$) indicate that the exchange interaction parameter at ambient pressure resides within the HL2 region. However, at pressures of 5 and 10 GPa, the results shift to the HL4 and AFM regions, respectively. This suggests that pressure induces concurrent increases in both the intralayer interaction J_3 and the interlayer interaction $J_2^{\perp}$, thereby causing a transition in the magnetic ground state from HL2 to eventual AFM under high-pressure conditions. This observation aligns with experimental findings, which note a transition to the AFM state above 7 GPa hydrostatic pressure. Of significant note, if the interlayer interaction remains constant and only the intralayer interaction J_3 is intensified, the magnetic state transitions exclusively from HL2 to HL1, without the potential to reach the AFM state. Consequently, we discern the substantial impact of the second-nearest neighbor interlayer interaction $J_2^{\perp}$, which competes with intralayer frustration and favors the AFM state. Additionally, MC simulations also indicate that under pressure, the sample undergoes transitions through the HL3 and HL4 states before ultimately reaching the AFM state. This observation suggests that these states with varying wave vectors ($\mathbf{q}$) may serve as intermediate states, a notion supported by the SHG observation around 6.5 GPa, as depicted in Fig. 3b.

In this study, we have presented a comprehensive investigation of the helimagnetic state of NiI_2 flakes under pressure using in situ high-pressure SHG and Raman spectroscopies. Our findings demonstrate a significant magnetic phase transition occurring at approximately 7 GPa, transitioning from a helimagnetic to antiferromagnetic state, accompanied by a marked increase in the magnetic transition temperature for both states. Our MC simulation and reported DFT results reveal a rapid strengthening of the interlayer second nearest-neighbor interaction under pressure, surpassing the intralayer exchange interaction. This change in interaction dynamics is pivotal, as it drives the transition from a helimagnetic to an antiferromagnetic state. The findings presented here have significant implications for understanding the fundamental properties of 2D magnetic materials and pave the way for their potential applications in next-generation magnetic devices.

Methods

Synthesis of NiI_2 single crystals: The high-quality NiI_2 single crystals studied in this paper were prepared by the chemical vapor transport method. The Ni powder (99.999%) and the transport agent I_2 pieces were placed in an alumina crucible with a molar ratio of Ni:I_2 = 1:1.5. After evacuated and sealed into a quartz tube, the crucible was placed into a single-zone tube furnace with the source temperature of 700 °C keeping for 7 days. A large number of millimeter-sized crystals were collected at the end of the quartz tube.

SHG measurement: the SHG measurements were conducted in a back-reflection geometry. The fundamental wave was generated from a Ti-Sapphire oscillator with an 80 MHz repetition rate and 150 fs pulse width. A wavelength of 880 nm was chosen for temperature-dependent SHG intensity and angular-resolved SHG measurements. The laser pulses were focused to a spot of around 2 μm on the sample at normal incidence using a 50× objective. The reflected SHG signal was collected by the same objective and detected by a spectrometer equipped with a thermoelectric-cooled charged-coupled device (CCD). A shortpass filter with a central wavelength of 650 nm was used to block the fundamental wave. For angular-resolved SHG measurements, a 1/2-wave plate with a wavelength range of 310–1100 nm is used to adjust the polarization of the fundamental wave. The reflected SHG signal passed through the same 1/2 waveplate and was divided into parallel and perpendicular components by a displacer. By rotating the fast axis of the 1/2 waveplate, the angular-resolved SHG in two orthogonal directions are obtained.

Raman measurement: Raman spectra were performed using a homemade micro-Raman system in the back-scattering geometry. A He-Ne laser at 633 nm was employed to excite NiI_2 samples, and the laser power was kept below 200 μW to avoid sample heating. The laser beam passed through three ultra-narrow bandpass filters, and was focused onto the NiI_2 samples by a 50× objective. The back-scattered light was collected by the same objective, passed through three narrow notch filters to suppress the Rayleigh scattering, and then was focused on the entrance slit of a spectrometer with 1800 grooves mm^{-1} diffraction grating and a nitrogen-cooled charge-coupled device (CCD).

Theoretical calculations

We conduct Monte Carlo (MC) simulations on an 14 × 14 × 12 three-dimensional triangular lattice with ABC stacking. The model Hamiltonian encompasses both isotropic and anisotropic exchange interactions. In our simulations, the intralayer nearest-neighbor interaction, denoted by J_1, is set to 1, serving as the energy unit. The intralayer nearest-neighbor anisotropic exchanges are set as follows: $J_{xx} = 0.1, J_{yy} = -0.12, J_{zz} = 0.03$, and $J_{yz} = 0.05$. Additionally, we consider two parameters for the intralayer next-next-nearest neighbor interaction J_3 and interlayer next-nearest neighbor interaction $J_2^{\perp}$. Furthermore, we maintain the magnitude of interlayer next-next-nearest neighbor interaction $J_3^{\perp}$ fixed at $0.35J_2^{\perp}$. The phase diagram is obtained through a three-stage process. Initially, we employ a combination of the parallel tempering method and heat-bath sampling

algorithm. Forty replicas of the system are simulated over a temperature range from $T = 0.01$ and $T = 4$, following a geometric progression. During this stage, we conduct 2×10^5 MC sweeps and exchange replicas after 100 sweeps. In the second stage, all replicas are quenched to a lower temperature of $T = 0.001$, followed by 10^5 heat-bath sweeps. Finally, we perform zero-temperature sampling, which involves aligning spins with the direction of their local effective field H_{eff} and employing an over-relaxation process, i.e., mirroring the spins according to H_{eff}. The ground states are then determined based on the lowest energy configurations among the 40 replicas.

Data availability

The data supporting this study's findings are available in the article and its Supplementary Information files. Source data are provided with this paper.

References

1. Gong, C. et al. Discovery of intrinsic ferromagnetism in two-dimensional van der Waals crystals. *Nature* **546**, 265–269 (2017).
2. Huang, B. et al. Layer-dependent ferromagnetism in a van der Waals crystal down to the monolayer limit. *Nature* **546**, 270–273 (2017).
3. Burch, K. S., Mandrus, D. & Park, J.-G. Magnetism in two-dimensional van der Waals materials. *Nature* **563**, 47–52 (2018).
4. Deng, Y. et al. Gate-tunable room-temperature ferromagnetism in two-dimensional Fe3GeTe2. *Nature* **563**, 94–99 (2018).
5. Fei, Z. et al. Two-dimensional itinerant ferromagnetism in atomically thin Fe3GeTe2. *Nat. Mater.* **17**, 778–782 (2018).
6. Jiang, P. et al. Stacking tunable interlayer magnetism in bilayer CrI_3. *Phys. Rev. B* **99**, 144401 (2019).
7. Sivadas, N., Okamoto, S., Xu, X., Fennie, C. J. & Xiao, D. Stacking-dependent magnetism in bilayer CrI3. *Nano Lett.* **18**, 7658–7664 (2018).
8. Wang, Z. et al. Very large tunneling magnetoresistance in layered magnetic semiconductor CrI3. *Nat. Commun.* **9**, 2516 (2018).
9. Subhan, F., Khan, I. & Hong, J. Pressure-induced ferromagnetism and enhanced perpendicular magnetic anisotropy of bilayer CrI3. *J. Phys. Condens. Matter* **31**, 355001 (2019).
10. Chen, W. et al. Direct observation of van der Waals stacking–dependent interlayer magnetism. *Science* **366**, 983–987 (2019).
11. Yang, S. et al. Controlling the 2D magnetism of CrBr3 by van der Waals stacking engineering. *J. Am. Chem. Soc.* **145**, 28184–28190 (2023).
12. Zheng, G. et al. Gate-tuned interlayer coupling in van der Waals ferromagnet Fe_3GeTe_2 nanoflakes. *Phys. Rev. Lett.* **125**, 047202 (2020).
13. Jiang, S., Li, L., Wang, Z., Mak, K. F. & Shan, J. Controlling magnetism in 2D CrI3 by electrostatic doping. *Nat. Nanotechnol.* **13**, 549–553 (2018).
14. Huang, B. et al. Electrical control of 2D magnetism in bilayer CrI3. *Nat. Nanotechnol.* **13**, 544–548 (2018).
15. Song, T. et al. Switching 2D magnetic states via pressure tuning of layer stacking. *Nat. Mater.* **18**, 1298–1302 (2019).
16. Li, T. et al. Pressure-controlled interlayer magnetism in atomically thin CrI3. *Nat. Mater.* **18**, 1303–1308 (2019).
17. Cheong, S.-W. & Mostovoy, M. Multiferroics: a magnetic twist for ferroelectricity. *Nat. Mater.* **6**, 13–20 (2007).
18. Liu, H. et al. Vapor deposition of magnetic Van der Waals NiI2 crystals. *ACS Nano* **14**, 10544–10551 (2020).
19. Billerey, D., Terrier, C., Ciret, N. & Kleinclauss, J. Neutron diffraction study and specific heat of antiferromagnetic NiI2. *Phys. Lett. A* **61**, 138–140 (1977).
20. Friedt, J. M., Sanchez, J. P. & Shenoy, G. K. Electronic and magnetic properties of metal diiodides MI2 (M=V, Cr, Mn, Fe, Co, Ni, and Cd) from 129I Mössbauer spectroscopy. *J. Chem. Phys.* **65**, 5093–5102 (2008).
21. Kuindersma, S. R., Sanchez, J. P. & Haas, C. Magnetic and structural investigations on NiI2 and CoI2. *Phys. B+C* **111**, 231–248 (1981).
22. Kurumaji, T. et al. Magnetoelectric responses induced by domain rearrangement and spin structural change in triangular-lattice helimagnets NiI${}_{2}$ and CoI${}_{2}$. *Phys. Rev. B* **87**, 014429 (2013).
23. Song, Q. et al. Evidence for a single-layer van der Waals multiferroic. *Nature* **602**, 601–605 (2022).
24. Jiang, Y. et al. Dilemma in optical identification of single-layer multiferroics. *Nature* **619**, E40–E43 (2023).
25. Wu, S. et al. Layer thickness crossover of type-II multiferroic magnetism in NiI2. *arXiv* https://doi.org/10.48550/arXiv.2307.10686 (2023).
26. Ju, H. et al. Possible persistence of multiferroic order down to bilayer limit of van der Waals material NiI2. *Nano Lett.* **21**, 5126–5132 (2021).
27. Li, X. et al. Realistic spin model for multiferroic NiI2. *Phys. Rev. Lett.* **131**, 036701 (2023).
28. Pizzocchero, F. et al. The hot pick-up technique for batch assembly of van der Waals heterostructures. *Nat. Commun.* **7**, 11894 (2016).
29. Pasternak, M. P. et al. Pressure-induced metallization and the collapse of the magnetic state in the antiferromagnetic insulator NiI_2. *Phys. Rev. Lett.* **65**, 790–793 (1990).
30. Giesekus, A. & Falicov, L. M. Theory of pressure-induced magnetic and metal-insulator transitions. *Phys. Rev. B* **44**, 10449–10454 (1991).
31. Pasternak, M. P., Taylor, R. D. & Jeanloz, R. in *Frontiers of High-Pressure Research* (eds Hochheimer, H. D. & Etters, R. D.) 227–241 (Springer, 1991).
32. Zhang, C. et al. Pressure-enhanced ferromagnetism in layered CrSiTe3 flakes. *Nano Lett.* **21**, 7946–7952 (2021).
33. Bhoi, D. et al. Nearly room-temperature ferromagnetism in a pressure-induced correlated metallic state of the van der Waals insulator $CrGeTe_3$. *Phys. Rev. Lett.* **127**, 217203 (2021).
34. Su, H. et al. Pressure-controlled structural symmetry transition in layered InSe. *Laser Photonics Rev.* **13**, 1900012 (2019).
35. Chen, A. L., Yu, P. Y. & Taylor, R. D. Closure of the charge-transfer energy gap and metallization of NiI_2 under pressure. *Phys. Rev. Lett.* **71**, 4011–4014 (1993).
36. Sugai, S. The pressure-induced metallic amorphous state of SnI4. II. Lattice vibrations at the crystal-to-amorphous phase transition studied by Raman scattering. *J. Phys. C Solid State Phys.* **18**, 799 (1985).
37. Connor, A. et al. Signatures of pressure-enhanced helimagnetic order in van der Waals multiferroic NiI2. *arXiv* https://doi.org/10.48550/arXiv.2306.11720 (2023).
38. Kapeghian, J. et al. Effects of pressure on the electronic and magnetic properties of bulk NiI2. *Phys. Rev. B* **109**, 014403 (2024).

Acknowledgements

We would like to thank Prof. Haizhou Lu from SUSTech for helpful discussions. J.W.M. acknowledges the support from the National Natural Science Foundation of China (Grant No. 12474143), the National Key Research and Development Program of China (Grant No. 2021YFA1400400), and Shenzhen Fundamental Research Program (Grant No. JCYJ20220818100405013 and JCYJ20230807093204010). J.F.D. acknowledges the support from the Guangdong Natural Science Foundation (2024A1515012679). The theoretical part was supported by the National Natural Science Foundation of China (11974197 and 51920105002), Guangdong Innovative and Entrepreneurial Research Team Program (No. 2017ZT07C341). C.R.W. acknowledges the support from Natural Science Foundation of Top Talent of SZTU (GDRC202434).

Author contributions

J.D. and J.M. conceived the project. J.D., Q.L., and W.S. designed and performed the experiments. X.Z., X.X., and L.W. provided and characterized the samples. N.Z. and M.H. conducted the Raman measurements under magnetic field. K.X., C.W. and X.C. provided SHG calculations and fitting. B.X., Y.G., X.L.Z., and J.M. provided the theoretical support. All authors discussed the results and co-wrote the paper.

Competing interests

The authors declare no competing interests.

Additional information

Supplementary information The online version contains supplementary material available at https://doi.org/10.1038/s41467-025-59561-0.

Correspondence and requests for materials should be addressed to Xiaolong Zou, Bin Xi, Jia-Wei Mei or Jun-Feng Dai.

Peer review information *Nature Communications* thanks Liuyan Zhao, and the other, anonymous, reviewer(s) for their contribution to the peer review of this work. A peer review file is available.

Reprints and permissions information is available at http://www.nature.com/reprints

Publisher's note Springer Nature remains neutral with regard to jurisdictional claims in published maps and institutional affiliations.

Open Access This article is licensed under a Creative Commons Attribution-NonCommercial-NoDerivatives 4.0 International License, which permits any non-commercial use, sharing, distribution and reproduction in any medium or format, as long as you give appropriate credit to the original author(s) and the source, provide a link to the Creative Commons licence, and indicate if you modified the licensed material. You do not have permission under this licence to share adapted material derived from this article or parts of it. The images or other third party material in this article are included in the article's Creative Commons licence, unless indicated otherwise in a credit line to the material. If material is not included in the article's Creative Commons licence and your intended use is not permitted by statutory regulation or exceeds the permitted use, you will need to obtain permission directly from the copyright holder. To view a copy of this licence, visit http://creativecommons.org/licenses/by-nc-nd/4.0/.

© The Author(s) 2025